

# Thermochemical Interaction of Thermal Barrier Coatings with Molten CaO–MgO–Al<sub>2</sub>O<sub>3</sub>–SiO<sub>2</sub> (CMAS) Deposits

Stephan Krämer,<sup>†</sup> James Yang, and Carlos G. Levi

Materials Department, University of California, Santa Barbara, Santa Barbara, California 93106-5050

Curtis A. Johnson

General Electric Global Research Center, Niskayuna, New York 12309

**Thermal barrier coatings (TBCs) are increasingly susceptible to degradation by molten calcium–magnesium aluminosilicate (CMAS) deposits in advanced engines that operate at higher temperatures and in environments laden with siliceous debris. This paper investigates the thermochemical aspects of the degradation phenomena using a model CMAS composition and ZrO<sub>2</sub>–7.6%YO<sub>1.5</sub> (7YSZ) grown by vapor deposition on alumina substrates. The changes in microstructure and chemistry are characterized after isothermal treatments of 4 h at 1200°–1400°C. It is found that CMAS rapidly penetrates the open structure of the coating as soon as melting occurs, whereupon the original 7YSZ dissolves in the CMAS and reprecipitates with a different morphology and composition that depends on the local melt chemistry. The attack is minimal in the bulk of the coating but severe near the surface and the interface with the substrate, which is also partially dissolved by the melt. The phase evolution is discussed in terms of available thermodynamic information.**

## I. Introduction

Thermal barrier coatings (TBC) are now fully recognized as enabling materials for enhancing the performance and durability of gas turbine engines,<sup>1,2</sup> a pre-eminent mode of propulsion technology as well as electricity generation and industrial power. In their coming of age, TBCs have had to overcome a reliability problem that limited their application to extending component life and precluded full exploitation of their capability for increasing gas path temperatures.<sup>3,4</sup> As confidence in their durability and reliability has grown, engine design has become increasingly dependent on TBCs for improving efficiency through higher operating temperatures. The ensuing benefits, however, have been accompanied by the emergence of new degradation and failure mechanisms. Notable among the latter is the attack by calcium–magnesium aluminosilicate (CMAS) deposits resulting from the ingestion of siliceous minerals (dust, sand, volcanic ash, runway debris) with the intake air, especially in aircraft engines.<sup>5</sup> At lower temperatures, these contaminants can cause erosive wear or local spallation of the TBC when impacting as solid particles.<sup>6–10</sup> As engine temperatures increase, the siliceous debris adheres to the TBC surfaces and yields glassy melts.<sup>11</sup> The latter can penetrate the micro-

structural features that induce compliance in the coating—microcracks in TBCs deposited by atmospheric plasma spray (APS) and columnar segmentation in those deposited by electron-beam physical vapor deposition (EB-PVD)—leading to a loss of strain tolerance.<sup>5</sup>

The envisaged damage mechanism involves exfoliation of discrete surface layers infiltrated with the molten CMAS as the latter freezes upon cooling and builds up stresses due to the thermal expansion mismatch with the substrate.<sup>5,12</sup> Recent work documented this damage mode<sup>13</sup> but also suggested that thermal shock may play a more important role in this mode of failure than the simple buildup of stress upon cooling. Nevertheless, the mechanism is essentially thermomechanical in origin and relevant to any molten deposit that penetrates the open spaces in the TBC and freezes within them. The extent of penetration is dictated by the interplay of the thermal gradient imposed across the thermal barrier with the fluidity of the melt. If siliceous debris continues to deposit on the surfaces exposed by the exfoliated layers, the process can be repeated until the TBC is removed.

Examination of coatings on engine parts subjected to CMAS reveals that there is also a thermochemical form of damage occurring at high temperature that further degrades the coating and could exacerbate the thermomechanical effects. Of the few studies available in the open literature, the earlier ones were primarily motivated by the concern that siliceous deposits would plug the cooling holes in airfoils and increase their temperature beyond tolerable limits,<sup>14</sup> with potential for hot corrosion of the metallic coating.<sup>15,16</sup> (These components were aluminized but did not have TBCs.) Stott *et al.* provided the first significant discussion of the corrosive effects of molten silicates on 7 wt% yttria-stabilized zirconia (7YSZ) TBCs.<sup>11,17,18</sup> Laboratory tests were performed by heating self-standing TBCs in contact with different sands for periods of 20–120 h at temperatures in the range 1400°–1500°C. Both APS and EB-PVD coatings were studied, but much of the discussion focused on APS. A salient claim was that YSZ dissolved in the silicate melt, preferentially along grain boundaries, and, depending on the melt chemistry, monoclinic ZrO<sub>2</sub> precipitated with a lower Y content.<sup>11</sup>

Studies on actual engine hardware with APS TBCs exposed to siliceous deposits focused on the occurrence of spallation as a result of coating infiltration by the melt and outlined the dominant failure regimes as a function of the TBC surface temperature.<sup>5</sup> A notable observation was that for seemingly disparate sources and overall compositions of mineral intake, the infiltrating melts were of similar composition and contained primarily CaO, MgO, Al<sub>2</sub>O<sub>3</sub>, and SiO<sub>2</sub>. Minor components of the melt included Fe and Ni, originating from the upstream engine metallic components, as well as Zr and Y from the TBC. Incipient melting temperatures for the deposits in this study were of order ~1200°C, whereas others reported temperatures as high as 1275°C<sup>11</sup> or as low as ~1136°C.<sup>16</sup> For reference, the lowest melting eutectics in the ternaries CaO–Al<sub>2</sub>O<sub>3</sub>–SiO<sub>2</sub>, CaO–MgO–

J. Smialek—contributing editor

Manuscript No. 21305. Received December 30, 2005; approved March 16, 2006.

Research sponsored by the Office of Naval Research under contracts N00014-99-1-0471 and MURI/N00014-00-1-0438, monitored by Dr. S. G. Fishman. The project benefited from the use of the UCSB-MRL Central Facilities supported by NSF under award No. DMR00-80034.

<sup>†</sup>Author to whom correspondence should be addressed. e-mail: skraemer@engineering.ucsb.edu

SiO<sub>2</sub>, and MgO–Al<sub>2</sub>O<sub>3</sub>–SiO<sub>2</sub> are 1170°, 1320°, and 1355°C, respectively, all involving silica (tridymite), the binary monosilicate (CS or MS), and a ternary silicate (CA<sub>2</sub>S<sub>2</sub>, CMS<sub>2</sub>, or M<sub>2</sub>A<sub>4</sub>S<sub>5</sub>)<sup>†</sup> (cf. figs. 630, 598, and 712 Levin *et al.*<sup>19</sup>). The lowest quaternary eutectic is reported at ~1150°C (cf. 908 Levin *et al.*<sup>19</sup>) and corresponds to the reaction L → S + MS + CMS<sub>2</sub> + CA<sub>2</sub>S<sub>2</sub>. A cursory analysis of the relevant phase equilibria literature suggests that silicate mixtures over a relatively broad composition range could have incipient melting points of order ~1200°C (especially when the effect of Fe is considered), comparable with expected surface temperatures for TBCs in state-of-the-art aero- and land-based engines. The CMAS problem is thus expected to become more pervasive as engine temperatures continue to increase in response to the demand for higher performance.

While there is evidence of thermochemical interactions between current TBC materials and molten CMAS, understanding of the ensuing corrosion mechanisms and resulting products is rather limited, especially for EB-PVD coatings. The present study aims to provide fundamental insight into these mechanisms with a focus on EB-PVD TBCs, which are arguably more susceptible to molten deposit penetration because of the open channels in their “segmented” microstructure. Experiments using a model CMAS composition on 7YSZ deposited on alumina substrates were used to explore the evolution of the TBC microstructure under controlled conditions. The results are discussed in light of available information on the relevant phase equilibria, outlining feasible paths leading to the evolution of the observed microstructures.

## II. Experimental Procedures

All TBC specimens comprised 7YSZ deposited by EB-PVD on polycrystalline alumina substrates (99.5% purity, CoorsTek, Golden, CO) using an in-house dedicated facility.<sup>20</sup> The use of ceramic substrates allows (i) the system to be heated isothermally above the melting point of the intended CMAS corrodent (>1200°C), which would cause excessive oxidation and microstructural degradation if superalloy substrates were used, and (ii) to assess the potential interactions if molten CMAS reaches the thermally grown aluminum oxide (TGO) in a TBC system. Conversely, the use of alumina substrates does not replicate the residual stresses that arise in the CMAS-infiltrated TBC on a superalloy substrate upon cooling, but such stresses and the related spallation phenomena were not the focus of the present study.

The 7YSZ sources were ceramic ingots, 25 mm diameter × 200 mm long, with ~38% porosity (Trans-Tech, Adamstown, MD). Major impurities reported (in weight percent) are 1.35HfO<sub>2</sub>, 0.08TiO<sub>2</sub>, 0.02SiO<sub>2</sub>, and ≤0.01 each of CaO, MgO, Al<sub>2</sub>O<sub>3</sub>, Fe<sub>2</sub>O<sub>3</sub>, Na<sub>2</sub>O, U, and Th. 200 μm thick coatings were deposited at ~2 μm/min on alumina substrates (25 mm × 25 mm × 0.6 mm) held at 1000°C and mounted on a tubular ceramic holder rotating over the source at a rate of 8 rpm to achieve the characteristic columnar, strain-tolerant microstructure desired in gas turbine applications.

The model CMAS selected had a chemical composition of 33CaO–9MgO–13AlO<sub>1.5</sub>–45SiO<sub>2</sub> or C<sub>33</sub>M<sub>9</sub>A<sub>13</sub>S<sub>45</sub> (all compositions henceforth in mole percent of single cation oxide formula units). It was based on the average of deposits on aircraft turboshaft shrouds operated in a desert environment, as reported Borom *et al.*,<sup>5</sup> excluding the minor components believed to originate mainly from the engine (Fe and Ni). The composition falls near the intersection of the primary crystallization domains for pseudowollastonite (α-CS), pyroxene/diopside (CMS<sub>2</sub>), melilite (C<sub>2</sub>MS<sub>2</sub>), and anorthite (CA<sub>2</sub>S<sub>2</sub>) in the quaternary liquidus projection (fig. 2647 Levin *et al.*<sup>21</sup>), with a crystallization temperature between 1200° and 1300°C. The CMAS was prepared by mixing reagent-grade fine powders of the individual oxides and

milling them in water to form a thick paste, which was subsequently applied to the surface of the TBC specimens to an area density of ~40 mg/cm<sup>2</sup>, well in excess of the amount estimated as needed to infiltrate all the porosity in the coating. After drying, the specimens were heated in a furnace to various temperatures in the range 1200°–1300°C, as well as 1400°C, and held in each case for 4 h. The nominal heating and cooling rate was 6°C/min.

Cross-sections of the as-deposited TBC and the various specimens exposed to CMAS were cut along a plane perpendicular to the rotation axis. These were embedded in epoxy and subsequently polished for examination by scanning electron microscopy (SEM) in both secondary (SE) and back-scattered electron (BSE) imaging modes, as well as by Raman spectroscopy. Transmission electron microscopy (TEM) specimens were cut from selected areas of the polished cross sections using a focused ion beam (FIB). This technique is particularly advantageous in case of the present specimens because it allows precise sampling of locations exhibiting specific microstructural features or reaction products. Chemical analysis was performed in both SEM and TEM using energy-dispersive X-ray spectroscopy (EDS).

## III. Results

The first notable observation is the abruptness with which CMAS penetrates and interacts with the TBC as soon as melting occurs. No evidence of melting, penetration, or even adhesion of the “deposit” to the coating surface was detected under 1230°C. Partial melting was noted at ~1235°C and completed by 1240°C, whereupon the TBC was fully impregnated and noticeably corroded by the CMAS after only 4 h. The excess contaminant on the surface had a glassy appearance with no residual solid and a few bubbles trapped upon cooling. Absent a gradient, the CMAS readily penetrated down to the substrate and visibly attacked it, as further elaborated below, promoting the detachment of parts of the TBC. The fracture surfaces along the rotation axis, where the segmentation in a pristine coating is most pronounced,<sup>20</sup> revealed that essentially all the intercolumnar gaps had been filled by CMAS and the TBC had consequently turned into a monolith upon cooling and lost its strain tolerance. The general features of the microstructure are similar at higher temperatures, with a concomitant increase in the severity of the interaction, as described below. Fewer bubbles appear trapped in the CMAS above 1300°C, presumably because of the concomitant decrease in melt viscosity.

The general appearance of the impregnated TBC is depicted in the polished cross section of Fig. 1, corresponding to the sample heated to 1300°C/4 h. The bulk of the coating appears to retain its columnar structure, albeit impregnated by CMAS, but two distinct interaction layers are evident at the interfaces with the bulk CMAS and the substrate. These are designated as the upper and lower interaction zones, respectively.

The features of the upper interaction zone are illustrated in Figs. 2 and 3. In this region, the columns lose their identity, with their characteristic tips (Fig. 2(a)) replaced by a conglomerate of much smaller globular particles embedded in CMAS (Fig. 2(b)). The relative proportion of phases is more clearly evident in the polished cross section of Fig. 2(c), where both seem to form interpenetrating networks. The upper reaction layer increases in thickness with temperature, from ~14 μm at 1240°C to ~21 μm at 1300°C and ~42 μm at 1400°C. However, its general appearance is relatively independent of temperature and quite similar to the equivalent region in a CMAS-degraded TBC on a service airfoil (Fig. 2(d)) even though the composition of the deposit is significantly different in the latter.<sup>22</sup> This gives confidence that the “model” CMAS replicates reasonably well the phenomena observed in real components, absent the thermal gradient.

TEM analysis (Fig. 3) reveals that the small globular particles in the top layer are fully dense, diverging substantially in appearance from the original columns (cf. Fig. 5). They are also monoclinic in nature and exhibit the twinned structure typical of the tetragonal → monoclinic martensitic transformation upon

<sup>†</sup>The abbreviated formulation adopted here is based on single cation oxide formula units, i.e., A = AlO<sub>1.5</sub>, C = CaO, M = MgO, S = SiO<sub>2</sub> and thus differs from that used conventionally in ceramics, based on the full oxide formula unit. Hence, CA<sub>2</sub>S<sub>2</sub> = CaAl<sub>2</sub>Si<sub>2</sub>O<sub>8</sub> (anorthite), CMS<sub>2</sub> = CaMgSi<sub>2</sub>O<sub>6</sub> (diopside), and M<sub>2</sub>A<sub>4</sub>S<sub>5</sub> = Mg<sub>2</sub>Al<sub>4</sub>Si<sub>5</sub>O<sub>18</sub> (cordierite).

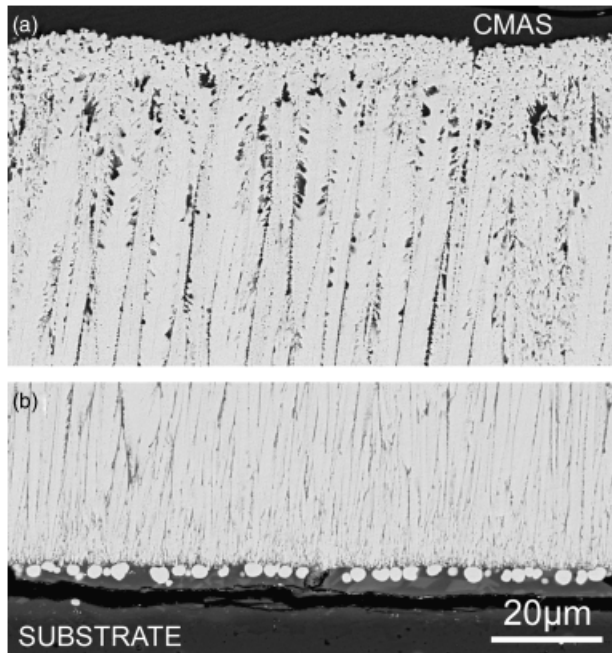


**Fig. 1.** Cross-section scanning electron microscopy images of a thermal barrier coatings (TBC) after exposure to calcium–magnesium aluminosilicate (CMAS) at 1300°C for 4 h, highlighting the regions of severe attack near the outer surface (a) and at the TBC/substrate interface (b). The residual CMAS on top, barely shown, is  $\sim 150 \mu\text{m}$  thick.

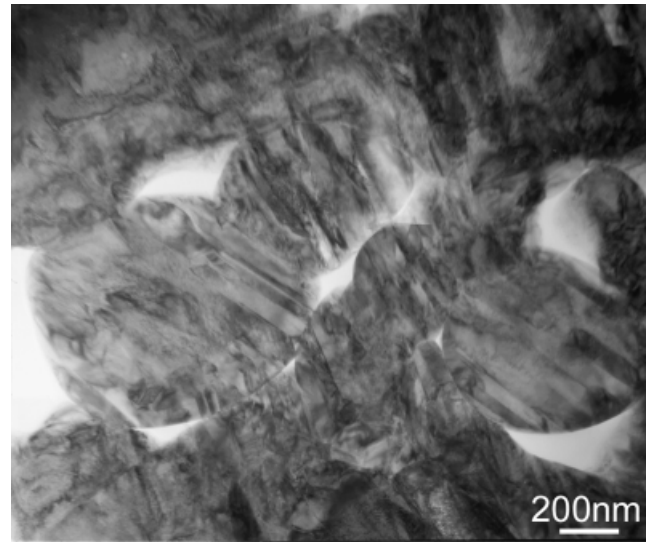


**Fig. 3.** Transmission electron microscopy image of the interaction zone in Fig. 2(b), where the classical martensitic structure produced by the tetragonal  $\rightarrow$  monoclinic transformation is clearly evident. Note that the globules are dense, and the intermediate spaces are filled with calcium–magnesium aluminosilicate.

cooling.<sup>23</sup> EDS analysis reveals that they have a lower  $\text{YO}_{1.5}$  content ( $< 3\%$ ) than the original 7YSZ and also incorporate some CaO ( $\sim 1\%$ ) in solid solution. The spaces within the particle network are filled with an amorphous phase, essentially identical in composition to the glassy bulk CMAS on top, both containing minor amounts of Zr and Y in addition to

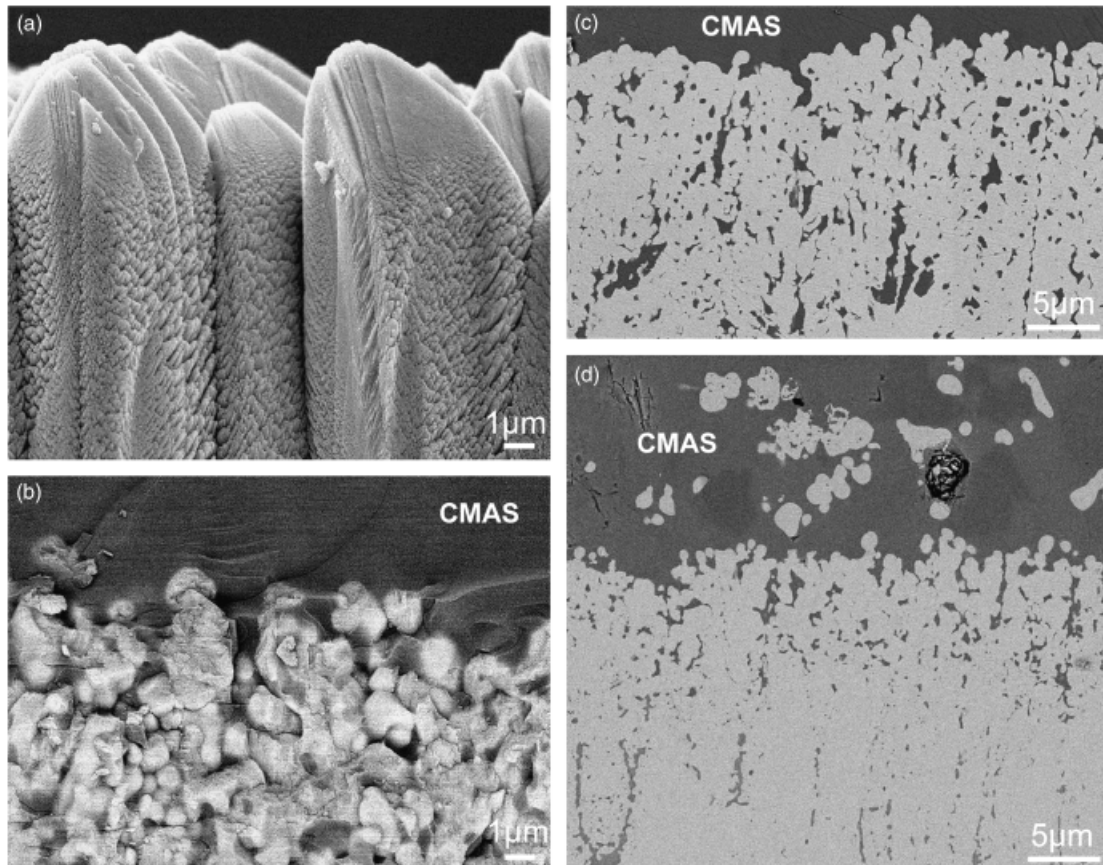


**Fig. 2.** Comparison of the column tips (a) in the pristine condition and (b, c) after exposure to the model calcium–magnesium aluminosilicate (CMAS) at 1300°C for 4 h (BSEI). The globular grains in (b) are about an order of magnitude smaller than the original column diameter and depleted in Y (Table I). They form a network interpenetrated by CMAS (c), and appear quite similar to structures observed near the surface of a thermal barrier coatings attacked by CMAS during actual engine operation (d).

**Table I. Chemical Compositions of Constituents in the Regions of the Interacting TBC-CMAS System. Values are given in mol%**

Region	Constituent	CaO	MgO	AlO <sub>1.5</sub>	SiO <sub>2</sub>	ZrO <sub>2</sub>	YO <sub>1.5</sub>
CMAS deposit		33	9	13	45		
Layer above TBC	CMAS	33	7	13	43	2	2
Prior column tips	CMAS	32	7	13	44	2	2
	Zirconia	1				98	2
Layer under corroded tips	CMAS	32	6	14	44	2	3
	Zirconia (column core)					92	8
Column roots	CMAS	32	7	9	46	3	3
	Zirconia					93	7
Reaction zone with substrate	CMAS	34	9	5	45	3	4
	Large globular zirconia	3				85	12
	Small YSZ particles	—				92	8
	Elongated crystals	22		33	43	2	—

TBC, thermal barrier coatings; CMAS, calcium–magnesium aluminosilicate; YSZ, yttria-stabilized zirconia.

the original components (Table I). The Y:Zr ratio in the CMAS is  $\sim 1$ , compared with  $\sim 1:12$  in the original TBC. An area EDS analysis in the SEM further revealed that the overall Y:Zr ratio in the upper reaction zone (amorphous+crystalline phases) is also lower than the original 7YSZ, consistent with the observation that significant amounts of Y and Zr migrated out into the large volume of molten CMAS above the coating.

Macroscopically, there is a relatively abrupt transition between the upper corrosion layer and the columnar structure retained through much of the underlying coating, although partially consumed column cores are often seen projecting into the globular structure at its lower boundary—e.g., Fig. 1(a). The transition is most clearly evident at the upper end of the narrower intercolumnar gaps, as in Fig. 4(a) where elongated bright pockets filled with CMAS delineate the boundary between two columns. The structure at the top is low in Y (Table I) and largely monoclinic (Fig. 4(b)). The porous structure and initial composition of the original column are still evident on the right-hand side in Fig. 4(c), but a thin layer of Y-depleted zirconia denoted by arrows has formed at the boundary between the column and the CMAS pocket. It could not be conclusively ascertained that this layer is monoclinic, but its Y content increases and its thickness disappears with increasing distance from the surface. Indeed, the cross-section  $\sim 1 \mu\text{m}$  above the column roots (Fig. 5(a)) shows little evidence of attack, manifested mostly by smoothing of the column surfaces and the presence of some Y and Zr in the amorphous phase (Table I). Higher magnification of these columnar sections (Fig. 5(b)) reveals that the fine-scale intracolumnar porosity remains largely unaffected and has not been penetrated by CMAS even though the intergranular pores are all impregnated. No monoclinic phase was detected in this region, and both the local and bulk Y:Zr ratios remain essentially at their original value.

The structure of the lower interaction zone in Fig. 6 is markedly different from the layers above. Four different constituents are detected in this figure. The brighter regions are Zr rich and appear in two distinct morphologies, namely large globules and smaller particles comparable in size with the roots of the TBC columns (most evident in Fig. 6(a)). The darker background contains two constituents of different composition, at least one seemingly crystalline with a faceted acicular or tabular morphology (Fig. 6(b)). The overall thickness of this zone increases with temperature, as seen by comparing the 1240° and 1300°C specimens in Figs. 6(a) and (b), respectively. All four constituents are present in both samples; the smaller Zr-rich particles are more abundant at the lower temperature (Fig. 6(a)) but the thinner reaction zone makes it more difficult to distinguish the darker constituents in the background.

TEM examination reveals the larger globular particles in Fig. 6 to be dense single crystals of cubic ZrO<sub>2</sub> (Fig. 7(b)) containing on average  $\sim 12\%$  YO<sub>1.5</sub> and  $\sim 3\%$  CaO (Table I). Conversely, the smaller crystals are *t'*-YSZ with the original

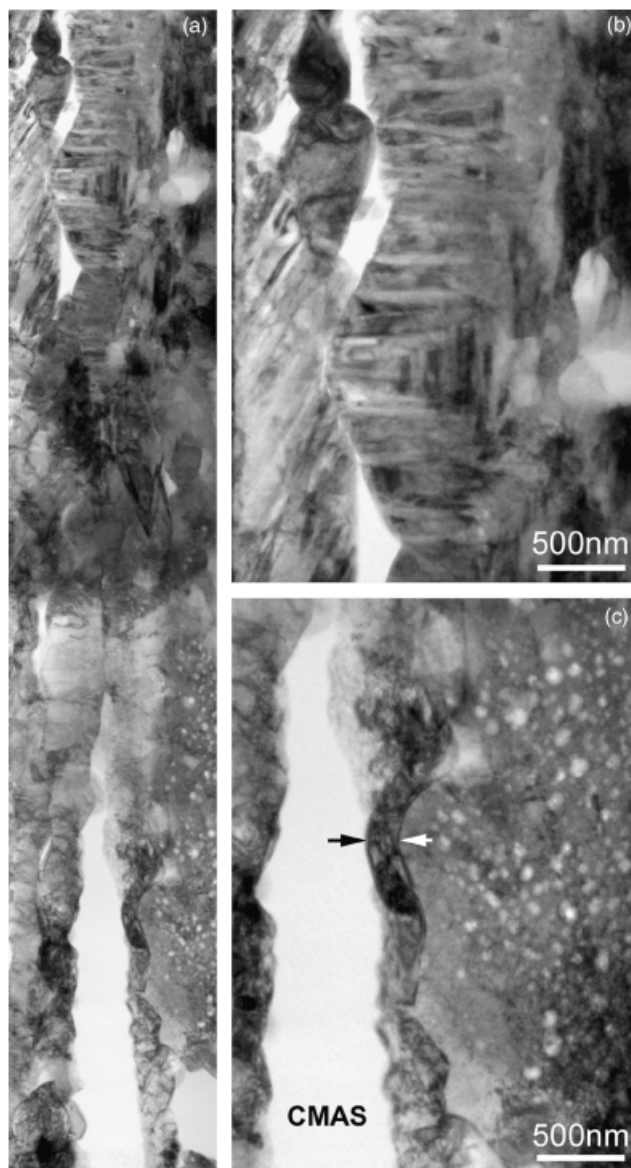


**Fig. 4.** Transmission electron microscopy images of the transition region at the bottom of the upper interaction layer in the specimen exposed to calcium–magnesium aluminosilicate (CMAS) at 1300°C for 4 h. (a) depicts the general view along a former intercolumnar gap, while (b) and (c) represent closer views of the top and bottom areas in (a). The structure in (b) exhibits the same martensitic appearance as Fig. 3. Conversely, the porous structure of the original column is still evident in (c), where a thin layer of Y-depleted yttria-stabilized zirconia, denoted by arrows, has formed at the interface with the CMAS pocket.

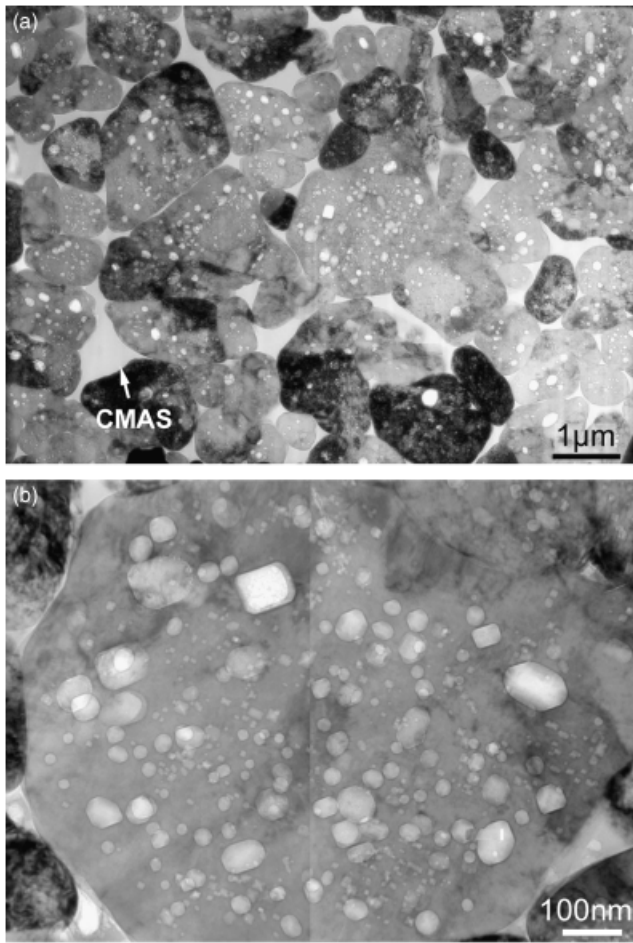


**Fig. 5.** Transmission electron microscopy views of the cross section of columns above the lower interaction zone, showing complete infiltration of the intercolumnar gaps by calcium–magnesium aluminosilicate (a) but no significant attack or Y-depleted layer (b). The columns retain their  $t'$  structure and original composition, as well as non-infiltrated intracolumnar porosity as shown in (b).

Y content and no incorporated Ca. No signs of monoclinic or Y-depleted zirconia were found, in contrast to the top part of the sample. It is further noted in Fig. 7(a) that the rounded roots of the  $t'$  columns (porous regions) suggest dissolution into the CMAS (glassy matrix) to feed the growth of the neighboring and much larger cubic grains. The composition of the glassy matrix is similar to that of the original CMAS, except for a lower Al content and the incorporation of minor amounts of Zr and Y (Table I). This matrix corresponds to the slightly brighter shade of gray in the background (Fig. 6(b)). The fourth and final constituent in Fig. 7(b) consists of large elongated crystals with Ca, Al, and Si in approximate ratios of 1:2:2, respectively (Table I). The chemistry and diffraction evidence are suggestive of anorthite ( $Ca_2Si_2O_7$ ), but the identity of this phase remains to be conclusively ascertained. The area EDS analysis across the lower interaction zone indicates that the average Y:Zr ratio is essentially the same as in the bulk of the columnar structure, in contrast with the upper layer that is significantly depleted in Y.

Raman spectroscopy confirmed that the local TEM observations are representative of the phase constitution in the relevant regions, as shown in Fig. 8. The characteristic signature of monoclinic around  $200\text{ cm}^{-1}$  appears down to  $\sim 20\text{ }\mu\text{m}$  (Fig. 8(b)) mixed with residual tetragonal, but not in the bulk of the coating (Fig. 8(c)) or at the lower interaction zone (Fig. 8(d)). The cubic phase does not have a particularly distinct Raman signature but its generalized presence along the interface is clearly evident in Fig. 1(b).

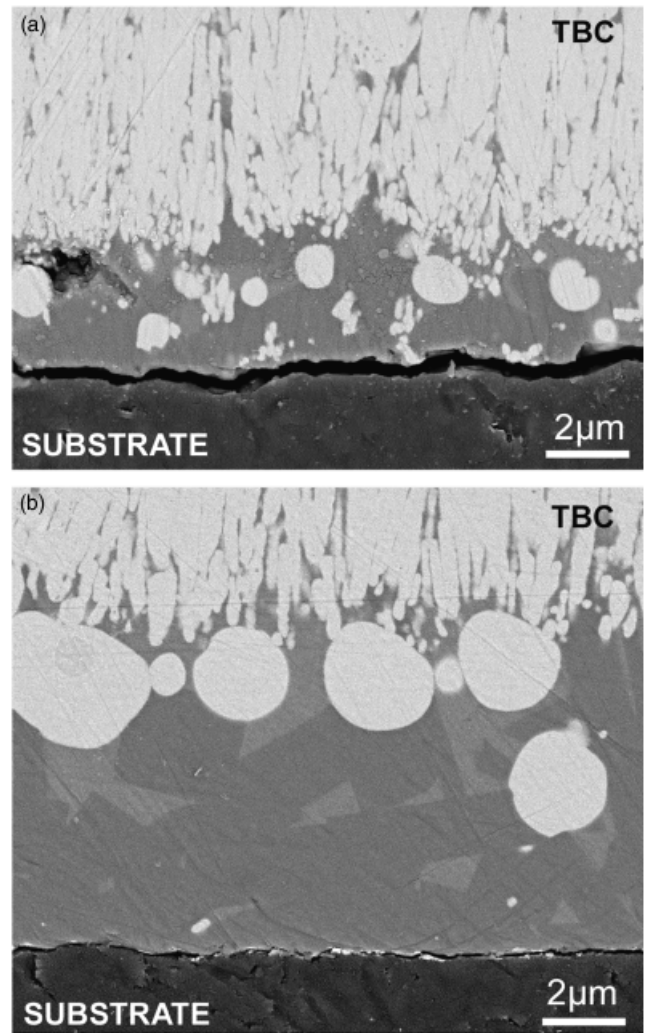


**Fig. 6.** Comparison of the lower interaction zones in the specimens heat treated at (a) 1240°C and (b) 1300°C, both for 4h (BSEI). Note the difference in scale between the initial column roots and the globules reprecipitated from the melt. The smaller bright particles, more evident in (a), are partially dissolved bits detached from the column roots. The darker faceted phase, more evident in (b), is an aluminosilicate tentatively identified as anorthite.

#### IV. Discussion

The following salient issues emerge from the above results: (i) CMAS rapidly and extensively infiltrates the TBC structure as soon as melting occurs; (ii) CMAS severely attacks the TBC at lower temperatures (1240°C) and in much shorter times (4 h) than those anticipated from previous reports in the literature<sup>11,17,18</sup>; (iii) CMAS obliterates the columnar morphology and converts the original  $t'$ -YSZ into monoclinic globular particles in the upper region of the coating, to a thickness that depends on temperature, but (iv) the attack is largely suppressed in the bulk of the TBC; and (v) it reactivates again at the bottom of the coating, where CMAS dissolves the alumina substrate and converts the original  $t'$  into larger cubic YSZ globules. These issues are discussed below.

##### (1) Infiltration Behavior

Examination of the infiltrated microstructures suggests that molten CMAS readily “wets” 7YSZ, spreading over the column surfaces and penetrating into any small open capillaries, e.g., those represented by the pristine “feathery” structure in Fig. 2(a). If the classical representation of wetting by a “contact

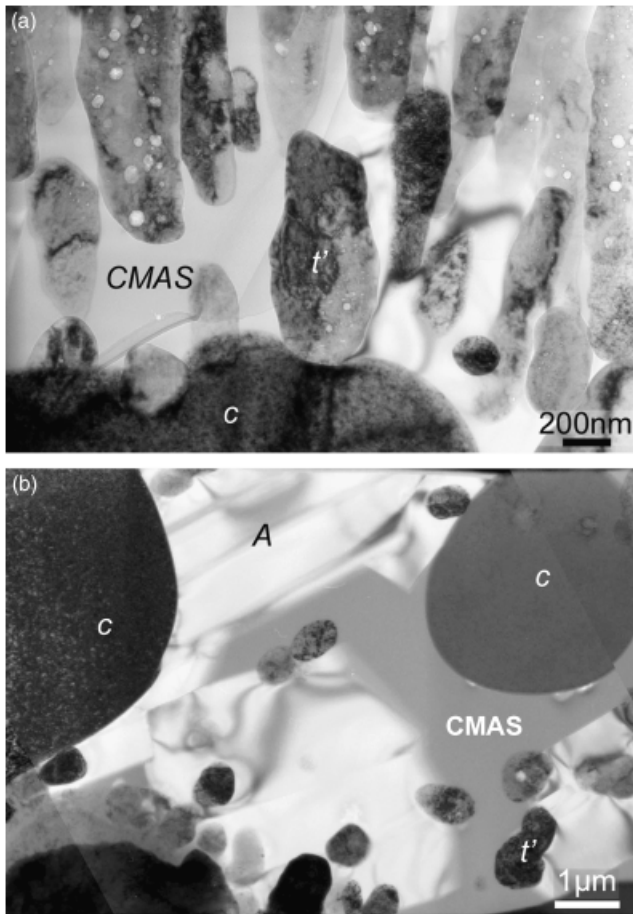


**Fig. 7.** Transmission electron microscopy images of the lower reaction zone in the specimen heat treated for 4 h at 1300°C showing (a) the roots of the  $t'$  columns right above the top of a large  $c$ -YSZ particle, and (b) the lower interaction zone comprising the reprecipitated cubic zirconia (large globules, marked “c”), the residual ( $t'$ ) YSZ bits, the crystalline aluminosilicate (A), and the residual glassy calcium–magnesium aluminosilicate background. YSZ, yttria-stabilized zirconia.

angle”  $\theta$  is invoked, the implication is that  $\theta$  is small and  $\cos(\theta \rightarrow 1$ .<sup>8</sup> Following standard treatments for the infiltration of porous media by fluids, the time needed for a wetting liquid ( $\cos\theta \rightarrow 1$ ) to penetrate to a depth  $L$  into the coating due to capillary action alone may be estimated as a first approximation from<sup>25</sup>:

$$t \approx \left[ \frac{k_t}{8D_c} \left( \frac{1-\omega}{\omega} \right)^2 L^2 \right] \frac{\eta}{\sigma_{LV}} \quad (1)$$

where  $\omega$  is the pore fraction open to flow (essentially the area fraction of intercolumnar gaps,  $\sim 0.1$ ),  $D_c$  is the capillary diameter ( $\sim 1 \mu\text{m}$ ),  $k_t$  is a tortuosity factor (1–10) reflecting the increased resistance to flow when the capillaries are not straight tubes,  $\eta$  is the viscosity of the fluid, and  $\sigma_{LV}$  is its surface tension. Note that the terms within the square brackets in Eq. (1) are only dependent on the geometry of the system, whereas the terms outside are only dependent on the fluid.

The viscosity and surface tension of silicate melts have been extensively studied in the literature. It is reported that  $\sigma_{LV}$  of silicate glasses at 1400°C may be estimated from the following expression<sup>26</sup>:

$$\sigma_{LV}(\text{mJ/m}^2) = 271.2 + 3.32[\text{CaO}] + 1.96[\text{MgO}] + 3.47[\text{Al}_2\text{O}_3] + K \quad (2)$$

<sup>8</sup>One can readily show from an interfacial energy balance that the infiltration of a melt originally deposited on a surface into open capillaries normal to it is always favored as long as  $\theta < \pi/2$ , (e.g., Brada and Clarke<sup>24</sup>), and thus near-ideal wetting ( $\theta \rightarrow 0$ ) is not required.

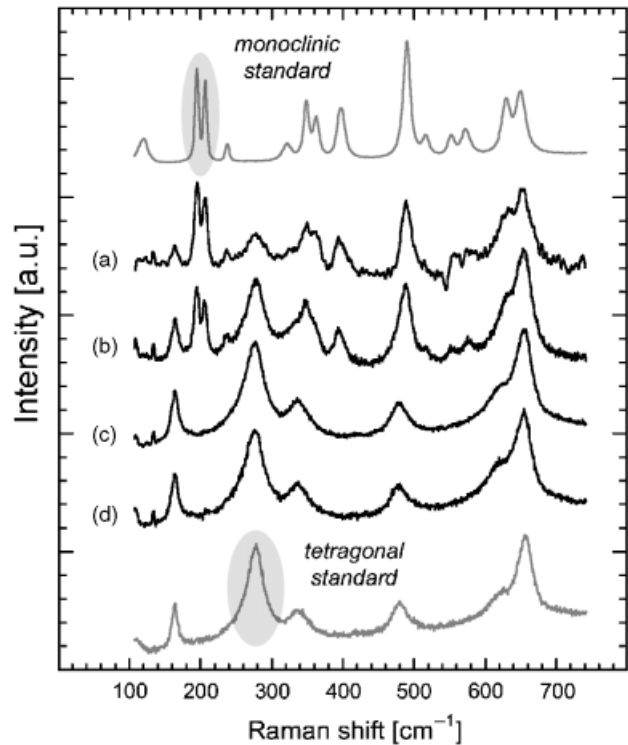


**Fig. 8.** Raman spectra taken from the polished cross section of the sample exposed to calcium–magnesium aluminosilicate (CMAS) at 1300°C/4 h, shown in Fig. 1. The positions correspond to (a) 5  $\mu\text{m}$  and (b) 20  $\mu\text{m}$  below the CMAS/TBC boundary; (c) middle of the TBC; and (d) at the lower interaction zone. The standard monoclinic and tetragonal patterns are given at the top and bottom of the figure. (The cubic pattern is not particularly distinct and not useful in this context.) TBC, thermal barrier coatings

where only the relevant oxides have been included here and all the concentrations are in mole percent. For the model CMAS melt in this study,  $\sigma_{LV}$  is then  $\sim 0.4 \text{ J/m}^2$ . (While some dependence on temperature is expected, the order of magnitude is not expected to change significantly within the range investigated.) The viscosities of CMAS can also be estimated from the chemical composition, as described in Turkdogan.<sup>27</sup> The resulting values at 1240°, 1300°, and 1400°C are  $\sim 15$ ,  $\sim 6$ , and  $\sim 2 \text{ N} \cdot (\text{s} \cdot \text{m}^2)^{-1}$ , respectively. On that basis and assuming  $k_t \sim 3$  for the intercolumnar gaps, one can estimate that the infiltration time for a 200  $\mu\text{m}$  coating would be less than 1 min even for the lowest temperature investigated. Moreover, at the rate of heating used in these experiments (6°C/min), the CMAS is expected to penetrate the coating down to the substrate shortly after melting, before the higher hold temperatures are reached. This explains in part why the attack at the TBC/substrate interface is substantial even at temperatures just above melting (1240°C).

Field experiences suggest that real CMAS could melt at even lower temperatures and, while its chemical composition may vary, the anticipated viscosities upon melting are expected to be similar in magnitude to the values above, and perhaps lower if significant amounts of other modifiers like FeO were incorporated.<sup>25</sup> Conversely, the thermal gradient would preclude penetration down to the TGO, although the infiltration front may not necessarily stop at the isotherm corresponding to the melting point when the melt does not crystallize upon cooling, as in the present case. These issues are currently under investigation.

## (2) CMAS Interactions with the TBC Columns

The three common crystallographic forms of YSZ are found present in the coating after exposure to CMAS, each in a different region and with a distinct morphology and Y content. Much of the coating away from the substrate and the exposed surface retains the initial  $t'$  structure and chemical composition

(~7.6%  $\text{YO}_{1.5}$ ), as well as the columnar morphology with nanoscale intragranular porosity, indicating that the thermochemical attack was minimal in these regions. However, the YSZ near the bulk CMAS deposit is monoclinic, depleted in Y, and that closest to the substrate is cubic, enriched in Y relative to the original composition. Minor amounts of Ca are incorporated into solid solution for both of these forms, but not to any detectable degree in the retained  $t'$  form. No other crystalline phases bearing major amounts of Zr or Y were found in the areas of the coating affected by CMAS.

The cumulative evidence suggests that both the Y-enriched and Y-depleted zirconia phases evolve through crystallization from the CMAS melt into which the original  $t'$  is concurrently dissolved, with the characteristics of the precipitated phase determined by the local chemistry. The situations for the bulk and upper regions are discussed first, as the lower interaction zone also involves the precipitation of a second crystalline phase based on  $\text{Al}_2\text{O}_3$  rather than  $\text{ZrO}_2$ . A complete analysis requires detailed knowledge of the phase equilibria in the system  $\text{Al}_2\text{O}_3$ - $\text{CaO}$ - $\text{MgO}$ - $\text{SiO}_2$ - $\text{Y}_2\text{O}_3$ - $\text{ZrO}_2$ , which is not available. The concept, however, can be illustrated qualitatively with the aid of the  $\text{CaO}$ - $\text{SiO}_2$ - $\text{ZrO}_2$  liquidus projection in Fig. 9. CMAS is represented by a binary liquid with the same C:S ratio (~0.73) in contact with  $\text{ZrO}_2$ , depicted by the tie line in this figure. At equilibrium, this composition should actually be solid below ~1430°C, consisting of a mixture of pseudowollastonite ( $\alpha$ -CS) and tridymite (fig. 10359 Roth<sup>28</sup>). However, the crystallization of these phases is often suppressed kinetically and one may reasonably assume that the composition selected may exist as a supercooled liquid with chemical characteristics similar to the CMAS melt. In that case, the actual boundary of the  $t$ - $\text{ZrO}_2$  liquidus would not be given by the position of the L+CS+Z twofold saturation line in Fig. 9, but shifted toward the C-S binary at temperatures below 1400°C, as indicated by the arrows. It is then readily apparent from Fig. 9 that the amount of Z needed to saturate the CS melt is quite modest (a few percent), in agreement with the  $\text{ZrO}_2$  content detected in much of the CMAS within the coating. A corollary is that the presence of

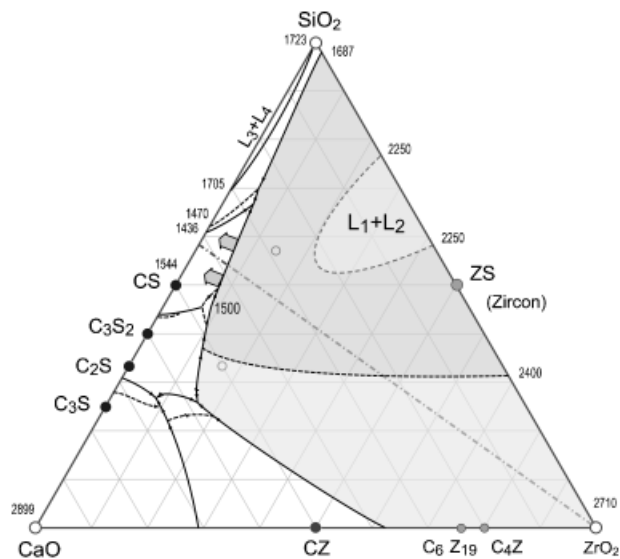


**Fig. 9.** Schematically modified liquidus projection for the ternary  $\text{CaO}$ - $\text{SiO}_2$ - $\text{ZrO}_2$ . The original diagram (fig. Zr-287 Ondik and McMurdie<sup>36</sup>), as many published around that time, ignores the existence of the cubic  $\leftrightarrow$  tetragonal transformation at high temperature as well as the existence of a two-phase miscibility gap in the liquid for the  $\text{SiO}_2$ - $\text{ZrO}_2$  binary. The schematic presented here incorporates qualitatively more recent evidence from partial isopleths and revised binaries. In general, the location of the relevant L+CS+Z two-phase saturation line on the liquidus is reasonably close to that in the original diagram. The tie line shown has the same C:S ratio as the model calcium-magnesium aluminosilicate.

$\text{MgO}$  and  $\text{Al}_2\text{O}_3$  in the original CMAS does not seem to affect substantially the solubility of  $\text{ZrO}_2$  in the melt.

The above scenario only explains the dissolution, but not the re-precipitation of YSZ with a different composition. The underlying driver in that case is the absence of equilibrium between the original YSZ composition and the initial melt, whereupon  $t'$ -YSZ would tend to dissolve and  $\text{ZrO}_2$  to precipitate back with a composition (lower in Y and with some Ca) that reduces the overall free energy of the system. The problem is conceptually analogous to the concurrent dissolution of  $\alpha$  and reprecipitation of  $\beta$  in the liquid-phase-assisted sintering of  $\text{Si}_3\text{N}_4$  ceramics,<sup>29</sup> with some important differences. First, the composition of the YSZ changes during the process but not its crystal structure, as inferred from the clear evidence that the monoclinic YSZ crystals of the upper interaction zone (Fig. 3(c)) evolved through a martensitic transformation of a tetragonal phase precipitated from the melt at the reaction temperature. This clarifies prior suggestions in the literature that the monoclinic phase forms directly from the melt.<sup>11\*</sup> A second notable difference is that the process is limited to the top layer. Evidently, the saturation limit for Zr is reached first near the dissolution interface, arguably providing a driving force for nucleation of Y-depleted  $t$ -YSZ at discrete points on the column surfaces. The differences in chemical potential within the melt in front of the  $t'$  parent phase and the new  $t$  precipitate continue to drive the dissolution of the former to feed the growth of the latter. (One may argue that precipitation could occur upon cooling but more extensive analysis of the progress of this mechanism, to be presented in a forthcoming publication, reveals that precipitation is actually occurring at temperature.) While the process should be conceptually identical within the intercolumnar spaces away from the surface, the melt volume is much smaller in this case and could reach equilibrium with precipitation of a minimal amount of depleted YSZ (detectable only at the upper end of the surviving columns, as noted in Fig. 4(c)). Conversely, the bulk CMAS on the surface is a large sink for the excess Y and allows the process to continue over the time scale of the experiment, gradually destroying the large columnar crystals and converting them into smaller globules.

The absence of penetration of the fine porosity within the columns in Figs. 4(c) and 5 indicates that the feathery porosity, clearly open near the tip (Fig. 2(a)), breaks down into closed pores before CMAS reaches the surface of the columns in those areas. This phenomenon may start during deposition, wherein the lower ends of the columns age *in situ* as the thickness continues to build up. However, the deposition temperature is rather modest, ~1000°C, and much of the evolution is likely to occur during the relatively slow heating to the CMAS melting temperature. Indeed, a sample exposed to a 1240°C/4 h treatment without CMAS (not shown) revealed substantial evolution of the feathery pores even at the top of the columns. The implication is that the extent of the globular upper zone may depend on the degree of aging of the TBC before contaminants deposit on it. This is currently under investigation.

### (3) CMAS Interactions at the TBC/Substrate Interface

In principle, the severity of attack should be comparable at the TBC/substrate interface and within the bulk coating if the relative volume fraction of CMAS remained similarly small. However, two important differences arise because of the attack of the substrate by the melt. The first one is a result of the ensuing local separation of the TBC from the substrate, driven by the combination of substrate dissolution and thermal mismatch stresses,<sup>11</sup> which allows further buildup of molten CMAS to form an

\*It is indeed possible to form monoclinic crystals directly from the melt, as observed in corrosion studies with sulfate-vanadate deposits,<sup>30</sup> but this occurs at lower temperatures (900°C) and the characteristics of the crystals are radically different from those in this study. Conversely, monoclinic can be observed even in the absence of CMAS due to the purely thermal destabilization of  $t'$ -YSZ at the more extreme combination of temperatures and times used Stott *et al.*,<sup>11</sup> as suggested by a variety of phase stability studies on TBCs.<sup>31-34</sup>

<sup>11</sup>Local separation of the coating from the substrate does not necessarily lead to a detachment of the attacked region. However, formation of the reaction zone did weaken the interface and resulted in cracking along the substrate interface upon cooling, as illustrated in Figs. 1 and 6. The cracked regions appeared to be sufficiently interlocked with the rest of the sample to avoid spallation.

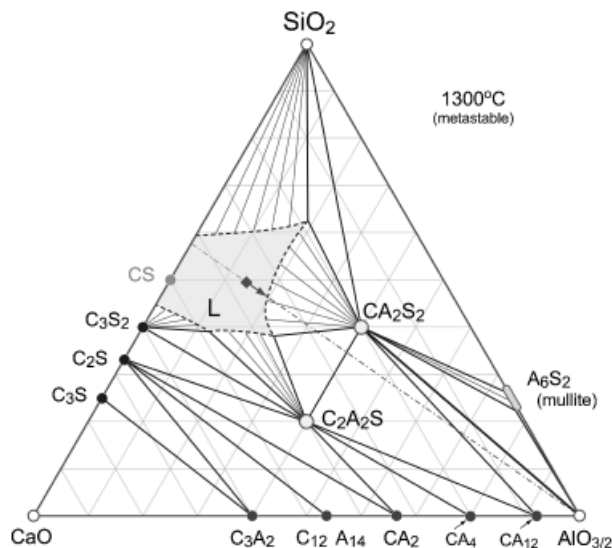


**Fig. 10.** Metastable isothermal cross section for the  $\text{AlO}_{1.5}\text{-CaO-SiO}_2$  system, based on fig. 630 Levin *et al.*<sup>19</sup> The pseudowollastonite liquidus has been suppressed whereupon the equilibrium liquid field has been extended metastably to the CaO-SiO<sub>2</sub> binary. The projection of the quaternary calcium-magnesium aluminosilicate (CMAS) composition onto this ternary is shown by the diamond symbol. The tie line between this composition and the alumina corner reflects the process that occurs when CMAS dissolves the alumina substrate and, upon saturation, precipitates anorthite ( $\text{CA}_2\text{S}_2$ ) at the lower interaction zone.

interfacial layer several times thicker than the typical intercolumnar gap. This would explain the reactivation of the dissolution-precipitation process when the CMAS reaches the bottom of the coating, but not the changes in the phase constitution and chemical composition of the precipitated zirconia. These are arguably linked to the injection of excess alumina into the melt and the subsequent precipitation of an aluminate crystalline phase.

Insight can be gained by examining first the reaction scenario for CMAS with the substrate absent YSZ. In this case, there is reasonable knowledge of the quaternary diagram but visualization is greatly enhanced by focusing on the CAS metastable ternary section in Fig. 10. It is assumed again that crystallization of the primary pseudowollastonite phase is kinetically suppressed, and hence the liquid region at 1300°C is metastably extended up to the C-S binary, as illustrated in Fig. 10. The projection of the quaternary CMAS composition onto the ternary is also marked in this figure, and a tie line representing the interaction with the alumina substrate is drawn to the corresponding corner of the diagram. The driver for dissolution-precipitation is immediately evident.  $\text{Al}_2\text{O}_3$  dissolves into the melt and shifts its composition toward the boundary of the anorthite ( $\text{CA}_2\text{S}_2$ ) + liquid field. After the requisite supersaturation is achieved to nucleate  $\text{CA}_2\text{S}_2$ , the system will tend to establish local equilibrium between anorthite and the melt, continuing to dissolve  $\text{Al}_2\text{O}_3$  and precipitate  $\text{CA}_2\text{S}_2$  as the overall composition shifts toward the  $\text{Al}_2\text{O}_3$  corner. It is further noted that the  $\text{Al}_2\text{O}_3$  content of the residual CMAS in the near-substrate region is significantly lower than that throughout the rest of the coating. The inference is that the anorthite crystals continued to grow upon cooling after the reaction hold, gradually depleting the liquid composition beyond the boundary indicated in Fig. 10, as expected from the slope of the liquidus surface in that region.

The physical characteristics of the anorthite and *c*-YSZ crystals suggest that both precipitate at temperature, although their sequence of nucleation is not completely clear. Nevertheless, the change in the local chemistry induced by the dissolution of alumina and reprecipitation of anorthite is arguably responsible for the shift in the redistribution pattern of Y and Zr upon crystallization of YSZ. The area EDS indicates that there is no significant change in the overall Y:Zr ratio relative to the original

coating, so the Y enrichment in *c*-YSZ is presumably compensated by the incorporation of Zr into the anorthite (Table I). It is also evident from the volume of cubic YSZ particles that, while significant, the extent of YSZ dissolution in this region is much smaller than that in the upper reaction layer, consistent with the lower volume of CMAS available. The survival of much of the column root structure (Fig. 7(a)) and small *t'* grains detached from this region into the CMAS melt (Figs. 6(a) and 7(b)) further supports the view that the dissolution rate is moderated by the incorporation of alumina. This suggests possible mitigation strategies that will be explored in subsequent publications.<sup>††</sup>

## V. Conclusions

The tendency of molten CMAS deposits to wet 7YSZ is sufficiently strong that columnar TBC structures can be infiltrated just above the onset of melting within times that are negligible compared with typical operation cycles of gas turbine engines. Infiltration is complete in isothermal exposures, but would be limited in a real operation to a depth dictated by the thermal gradient across the coating and the viscosity of the melt.

Thermochemical interactions between CMAS and the TBC occur at lower temperatures (1240°C) and shorter times (<4 h) than suggested by previous studies in the literature. In general, the mechanism involves dissolution of the metastable *t'* phase and re-precipitation with a composition and structure that depends on the local chemistry. Interactions in the bulk of the coating are minimized by the small volume of melt in relation to the amount of TBC material. Where larger volumes of CMAS are available, as in the near-surface region, the reprecipitated YSZ is sufficiently depleted in Y that it transforms to monoclinic upon cooling. The associated volume change could, in principle, contribute to the strains that motivate exfoliation of the coating upon thermal cycling. Near the substrate, the local chemistry is different due to the dissolution of the underlying alumina by the CMAS, inducing precipitation of a crystalline aluminosilicate and globules of a Y-enriched, non-transformable cubic YSZ.

The present study suggests a number of relevant research directions, ranging from understanding of the early stages of interaction, the effect of varying CMAS chemistry in the rate of dissolution and the nature of the crystalline products, the sequence in which these products evolve, and the potential implications for the mitigation of CMAS attack on thermal barrier coatings. These issues are presently under investigation and will be discussed in forthcoming publications.

## Acknowledgments

Enlightening discussions with Prof. A. G. Evans and Ms. S. Faulhaber (UCSB), as well as Drs. R. Darolia, B. Nagaraj, M. Gorman, D. Wortman (GE-Aviation), and M. Thompson (GE-Global Research) are gratefully acknowledged.

## References

- Schafrik and R. Sprague, "Saga of Gas Turbine Materials, Part III," *Adv. Mater. Processes*, **162** [5] 29–33 (2004).
- C. G. Levi, "Emerging Materials and Processes for Thermal Barrier Systems," *Curr. Opin. Solid State Mater. Sci.*, **8** [1] 77–91 (2004).
- P. K. Wright and A. G. Evans, "Mechanisms Governing the Performance of Thermal Barrier Coatings," *Curr. Opin. Solid State Mater. Sci.*, **4**, 255–65 (1999).
- A. G. Evans, D. R. Mumm, J. W. Hutchinson, G. H. Meier, and F. S. Pettit, "Mechanisms Controlling the Durability of Thermal Barrier Coatings," *Prog. Mater. Sci.*, **46** [5] 505–53 (2001).
- M. P. Borom, C. A. Johnson, and L. A. Peluso, "Role of Environmental Deposits and Operating Surface Temperature in Spallation of Air Plasma Sprayed Thermal Barrier Coatings," *Surf. Coatings Technol.*, **86–87**, 116–26 (1996).
- J. R. Nicholls, M. J. Deakin, and D. S. Rickerby, "A Comparison Between the Erosion Behavior of Thermal Spray and Electron-Beam Physical Vapour Deposition Thermal Barrier Coatings," *Wear*, **233–235**, 352–61 (1999).

<sup>††</sup>Approaches to control CMAS infiltration by providing a sacrificial layer of  $\text{Al}_2\text{O}_3$  on the TBC surface have been proposed in the patent literature,<sup>35</sup> but the rationale is based primarily on promoting crystallization to reduce penetration into the coating, rather than mitigation of the thermochemical attack.

- <sup>7</sup>R. G. Wellman and J. R. Nicholls, "A Mechanism for the Erosion of EB PVD TBCs," *Mater. Sci. Forum*, **369-372** [Part 1] 531-8 (2001).
- <sup>8</sup>X. Chen, R. Wang, N. Yao, A. G. Evans, J. W. Hutchinson, and R. W. Bruce, "Foreign Object Damage in a Thermal Barrier System: Mechanisms and Simulations," *Mater. Sci. Eng.*, **A352** [1-2] 221-31 (2003).
- <sup>9</sup>X. Chen, M. Y. He, I. T. Spitsberg, N. A. Fleck, J. W. Hutchinson, and A. G. Evans, "Mechanisms Governing the High Temperature Erosion of Thermal Barrier Coatings," *Wear*, **256** [7-8] 735-46 (2004).
- <sup>10</sup>A. G. Evans, N. A. Fleck, S. Faulhaber, N. Vermaak, M. Maloney, and R. Darolia, "Scaling Laws Governing the Erosion and Impact Resistance of Thermal Barrier Coatings," *Wear*, **260** [7-8] 886-94 (2006).
- <sup>11</sup>F. H. Stott, D. J. de Wet, and R. Taylor, "Degradation of Thermal-Barrier Coatings at Very High Temperatures," *MRS Bull.*, **19** [10] 46-9 (1994).
- <sup>12</sup>R. Darolia and B. A. Nagaraj, "Method of Forming a Coating Resistant to Deposits and Coating Formed Thereby"; U.S. Patent 6,720,038, 2004.
- <sup>13</sup>C. Mercer, S. Faulhaber, A. G. Evans, and R. Darolia, "A Delamination Mechanism for Thermal Barrier Coatings Subject to Calcium-Magnesium-Alumino-Silicate (CMAS) Infiltration," *Acta Mater.*, **53** [4] 1029-39 (2005).
- <sup>14</sup>J. Kim, M. G. Dunn, A. J. Baran, D. P. Wade, and E. L. Tremba, "Deposition of Volcanic Materials in the Hot Sections of Two Gas Turbine Engines," *J. Eng. Gas Turbines Power*, **115** [7] 641-51 (1993).
- <sup>15</sup>J. L. Smialek, F. A. Archer, and R. G. Garlick, "The Chemistry of Saudi Arabian Sand: A Deposition Problem on Helicopter Turbine Airfoils"; in *3rd International SAMPE Metals and Metals Processing Conference*, Edited by T.S. Reinhart, M. Rosenow, R.A. Cull, and E. Struckholt. Society for the Advancement of Material and Process Engineering (SAMPE), Toronto, Canada, 1992.
- <sup>16</sup>J. L. Smialek, F. A. Archer, and R. G. Garlick, "Turbine Airfoil Degradation in the Persian Gulf War," *J. Min. Metal. Mater. Soc.*, **46** [12] 39-41 (1994).
- <sup>17</sup>F. H. Stott, D. J. de Wet, and R. Taylor, "The Effect of Molten Silicate Deposits on the Stability of Thermal Barrier Coatings for Turbine Applications at Very High Temperatures"; in *3rd International SAMPE Metals and Metals Processing Conference*, Edited by T.S. Reinhart, M. Rosenow, R.A. Cull, and E. Struckholt. Society for the Advancement of Material and Process Engineering (SAMPE), Toronto, Canada, 1992.
- <sup>18</sup>D. J. de Wet, R. Taylor, and F. H. Stott, "Corrosion Mechanisms of ZrO<sub>2</sub>-Y<sub>2</sub>O<sub>3</sub> Thermal Barrier Coatings in the Presence of Molten Middle-East Sand," *J. Phys. IV*, **3** [C9] 655-63 (1993).
- <sup>19</sup>E. M. Levin, C. R. Robbins, and H. F. McMurdie, eds. *Phase Diagrams for Ceramists*, Vol. I, pp. 210, 219, 246. The American Ceramic Society, Columbus, OH, 1964.
- <sup>20</sup>S. G. Terry, "Evolution of Microstructure During the Growth of Thermal Barrier Coatings by Electron-Beam Physical Vapor Deposition"; Doctoral Dissertation in Materials, University of California, Santa Barbara, CA, 2001.
- <sup>21</sup>E. M. Levin, C. R. Robbins, and H. F. McMurdie, eds. *Phase Diagrams for Ceramists*, Vol. II, p. 185. The American Ceramic Society, Columbus, OH, 1969.
- <sup>22</sup>S. Krämer and S. Faulhaber. Work in progress, to be published.
- <sup>23</sup>M. Rühle and A. H. Heuer, "Phase Transformations in ZrO<sub>2</sub>-Containing Ceramics: II, the Martensitic Reaction in t-ZrO<sub>2</sub>"; pp. 14-32 in *Science and Technology of Zirconia II*, Edited by N. Claussen, M. Rühle, and A. H. Heuer. The American Ceramic Society, Columbus, OH, 1984.
- <sup>24</sup>M. P. Brada and D. R. Clarke, "A Thermodynamic Approach to the Wetting and De-Wetting of Grain Boundaries," *Acta Mater.*, **45** [6] 2501-8 (1997).
- <sup>25</sup>D. R. Poirer and G. H. Geiger, *Transport Phenomena in Materials Processing*. The Minerals, Metals and Materials Society, Warrendale, PA, 1994.
- <sup>26</sup>A. Kucuk, A. G. Clare, and L. Jones, "An Estimation of the Surface Tension of Silicate Glass Melts at 1400°C Using Statistical Analysis," *Glass Technol.*, **40** [5] 149-53 (1999).
- <sup>27</sup>E. T. Turkdogan, *Physical Chemistry of High Temperature Technology*. Academic Press, New York, 1980.
- <sup>28</sup>R. S. Roth, ed. *Phase Equilibria Diagrams, Volume XIII: Oxides*, p. 91. The American Ceramic Society, Westerville, OH, 2001.
- <sup>29</sup>P. Drew and M. H. Lewis, "The Microstructures of Silicon Nitride Ceramics During Hot-Pressing Transformations," *J. Mater. Sci.*, **9**, 261-9 (1974).
- <sup>30</sup>F. M. Pitek, S. Krämer, and C. G. Levi. Work in progress, to be published.
- <sup>31</sup>R. A. Miller, J. L. Smialek, and R. G. Garlick, "Phase Stability in Plasma-Sprayed, Partially Stabilized Zirconia-Yttria"; pp. 241-53 in *Science and Technology of Zirconia*, Edited by A. H. Heuer and L. W. Hobbs. The American Ceramic Society, Inc., Columbus, OH, 1981.
- <sup>32</sup>U. Schulz, "Phase Transformation in EB-PVD Yttria Partially Stabilized Zirconia Thermal Barrier Coatings During Annealing," *J. Am. Ceram. Soc.*, **83** [4] 904-10 (2000).
- <sup>33</sup>N. R. Rebollo, "Phase Stability of t'-Zirconia with Trivalent Oxide Additions for Use in Thermal Barrier Coatings"; Doctoral Dissertation in Materials, University of California, Santa Barbara, CA, 2005.
- <sup>34</sup>V. Lughì and D. R. Clarke, "High Temperature Aging of YSZ Coatings and Subsequent Transformation at Low Temperature," *Surf. Coatings Technol.*, **200** [5-6] 1287-91 (2005).
- <sup>35</sup>W. C. Hasz, C. A. Johnson, and M. P. Borom, "Protection of Thermal Barrier Coating by a Sacrificial Surface Coating"; U.S. Patent 5,660,885, 1997.
- <sup>36</sup>H. M. Ondik, and H. F. McMurdie, eds. *Phase Diagrams for Zirconium and Zirconia Systems*, p. 198. The American Ceramic Society, Westerville, OH, 1998.

□